OPEN ACCESS
IOP Publishing
Modelling and Simulation in Materials Science and Engineering
Modelling Simul. Mater. Sci. Eng. **33** (2025) 045016 (15pp) https://doi.org/10.1088/1361-651X/add950

Some notes about simulating nanoindentation with imperfect Berkovich tip

Karol Frydrych

[1] NOMATEN Centre of Excellence, National Centre for Nuclear Research Sołtana 7, 05-400 Otwock, Poland
[2] Institute of Fundamental Technological Research, Polish Academy of Sciences Pawińskiego 5b, 02-106 Warsaw, Poland

E-mail: karol.frydrych@ncbj.gov.pl

Received 14 January 2025; revised 10 April 2025
Accepted for publication 15 May 2025
Published 27 May 2025

Abstract
The article highlights the importance of correct treatment of indenter tip when modelling Berkovich nanoindentation. In order to account for tip imperfection, a novel analytical function describing the shape of Berkovich tip has been proposed. The parameters of the constitutive model were calibrated using experimental stress–strain curves. Simulations of Berkovich indentation with the same set of constitutive model parameters have been then conducted. An agreement between simulated and experimental stress–strain curves as well as load-displacement curves with a single set of constitutive model parameters has been demonstrated. Finally, the role of imperfection size and crystallographic orientation have been discussed.

Keywords: Berkovich indentation, crystal plasticity, finite element method, modelling nanoindentation, tip imperfection

1. Introduction

The tip invented by Berkovich [1] is now widely used in experimental indentation tests [2, 3]. However, from the point of view of finite element method (FEM) simulations of the instrumented indentation test, it is far easier to consider contact with a rigid spherical indenter as it

Original Content from this work may be used under the terms of the Creative Commons Attribution 4.0 licence. Any further distribution of this work must maintain attribution to the author(s) and the title of the work, journal citation and DOI.

© 2025 The Author(s). Published by IOP Publishing Ltd

can be simply modelled analytically as a rigid body, see [4–6]. While the perfect Berkovich tip can be also easily treated analytically [7, 8] or by meshing the perfect pyramid [9, 10], it was already shown in multiple papers that the tip bluntness can change the measured response considerably.

Even for the *conical* indenter, it was shown in [11] that in the case of the isotropic elastic perfectly plastic material, the hardness varies appreciably in the depth range comparable to the indenter tip. Sakharova *et al* performed simulations of indentation with Berkovich, Vickers and conical tips [12]. Parametric Bézier curves were applied to account for tip imperfection, however, the effect of the imperfection size was not studied.

The influence of the Berkovich tip defect radius on the load-displacement (LD) curves was analysed already in [13]. For the analysed case of elasto-plastic material with power law strain hardening (with rather low work hardening), the analysis showed only small though noticeable variations in load level at a given displacement. Kovar *et al* [14] performed simulations of the bilinear material (fused silica) subjected to indentation with *Berkovich* indenter. The authors considered not only roundness of the tip but also of the indenter edges. They demonstrated that increasing roundness from 0 (perfectly sharp indenter) through 100, 200 and 400 up to 800 nm leads to increased steepness of the force-displacement curves (maximal force was attained with 800 nm roundness). The effect of tip roundness was also examined in [15]. The radius of tip curvature was measured using atomic force microscopy (AFM) to be 933 nm and this value was used in simulations. The investigated material was again fused silica, this time with isotropic elasto-plastic behaviour. Taking the roundness into account resulted in a huge increase of the load at given depth. The residual imprint obtained in FEM simulation was consistent with the one observed using AFM.

Krier *et al* [16] attempted to reproduce the real geometry of the Berkovich indenter in an even more detailed fashion. They have considered two Berkovich indenters with small and high tip defects, whose surfaces were imaged using AFM. Then both indenter scans were turned into a volume and meshed. The authors reported significant changes in LD curves when comparing simulations with AFM-measured tips and the perfectly sharp tips. AFM-measured Berkovich tip surface was also directly used to perform FEM simulations in [17]. The authors showed that worn Berkovich indenter is rounded not only in the tip region, but also on the edges. For the case of the linear isotropic elastic material and very low penetration depth (about 20 nm) they considered, the material's response obtained with AFM-based shape was only slightly harder than the one obtained with the axisymmetric sphero-conical indenter.

Sanchez-Camargo *et al* [18] performed simulations with the Berkovich indenter constructed based on the area function obtained using the Oliver-Pharr method. The authors reported significant differences in LD curves obtained using the tip as modelled in their paper and the sharp tip used for comparison.

However, there is yet no systematic study of the effect of Berkovich tip roundness in the case of crystal plasticity. The aim of the present paper is to partially fill this gap. The article is structured as follows. After this introductory section, the next section 2 describes the aspects of the crystal plasticity framework, idealization of Berkovich indenter tip surface and the procedure to calibrate the constitutive model parameters. Then, the next section 3 presents the results of the Berkovich nanoindentation simulations compared against experimental data. Discussion (section 4) touches upon the effects related to size of the imperfection radius and crystal orientation. The paper ends with conclusions.

2. Modelling and simulations

2.1. Crystal plasticity finite element method

The model is defined in the finite strain, total Lagrangian framework. The kinematics was implemented in the same way as in [4, 19, 20] and is here only briefly described for the sake of completeness. Deformation gradient $\mathbf{F}$ is decomposed into elastic and plastic parts:

$$\mathbf{F} = \mathbf{F}_e \mathbf{F}_p, \tag{1}$$

and the plastic part of the velocity gradient $\hat{\mathbf{L}}_p$ defines the evolution of the plastic part of deformation gradient:

$$\dot{\mathbf{F}}_p = \hat{\mathbf{L}}_p \mathbf{F}_p. \tag{2}$$

$\hat{\mathbf{L}}_p$ is itself defined as a sum of shears on slip systems:

$$\hat{\mathbf{L}}_p = \sum_{r=1}^{M} \dot{\gamma}^r \mathbf{m}_0^r \otimes \mathbf{n}_0^r. \tag{3}$$

The classical power law [21] is used to obtain shear rate on each slip system r:

$$\dot{\gamma}^r = v_0 \mathrm{sign}\left(\tau^r\right) \left| \frac{\tau^r}{\tau_c^r} \right|^n. \tag{4}$$

The resolved shear stress (RSS) is obtained as a projection of the Mandel stress tensor:

$$\tau^r = \mathbf{m}_0^r \cdot \mathbf{M}_e \cdot \mathbf{n}_0^r, \tag{5}$$

which itself is obtained using the hyper-elastic law:

$$\mathbf{M}_e = 2\mathbf{C}_e \frac{\partial \Psi}{\partial \mathbf{C}_e}. \tag{6}$$

The free energy density of the form:

$$\Psi = \frac{1}{2} \mathbf{E}_e \cdot \mathbb{C}_e \cdot \mathbf{E}_e \tag{7}$$

is used. In (7), $\mathbf{E}_e$ is the elastic Lagrangian strain tensor:

$$\mathbf{E}_e = \frac{1}{2}\left(\mathbf{C}_e - \mathbf{1}\right) \tag{8}$$

and $\mathbb{C}_e$ is the stiffness tensor. On the other hand, $\mathbf{C}_e$ present in equation (8) is the right elastic Cauchy-Green tensor:

$$\mathbf{C}_e = \mathbf{F}_e^T \mathbf{F}_e. \tag{9}$$

The rest of the formulation is *clearly different from the formulations we previously used* e.g. in [19, 20, 22, 23]. Namely, here we apply a dislocation density based crystal plasticity (DDCP) model building upon the formulation developed for austenitic stainless steels [24–26]. Note that the original model accounted also for irradiation defects, but in this paper, we omit

Table 1. The components of the matrix h_τ as specified in equation (18) [24, 25].

$a1$	$a2$	$a3$	$a4$	$a5$	$a6$
0.124	0.124	0.07	0.625	0.137	0.122

the irradiation hardening terms as we use the model for material in the virgin state. Concerning the critical resolved shear stress (CRSS) τ_c^s on a given slip system s, it consists of two terms, a friction stress τ_0 (constant w.r.t. the deformation) and a term directly depending on the density of dislocations:

$$\tau_c^s = \tau_0 + \mu b_D \sqrt{\sum_u^{12} h_\tau^{su} \rho_D^u}. \tag{10}$$

The form of the matrix h_τ^{su} is specified in the appendix, while the components of the matrix h_τ^{su} are defined in table 1.

The evolution of dislocation densities is governed by the multiplication-annihilation law as follows:

$$\dot{\rho}_D^s = \frac{1}{b_D}\left(\frac{\sqrt{\sum_u^{12} h_\rho^{su}\rho_D^u}}{\kappa} - y_c b_D \rho_D^s\right)|\dot{\gamma}| \tag{11}$$

where the matrix h_ρ^{su} is defined as:

$$h_\rho^{su} = 1 - \delta^{su}, \tag{12}$$

where δ^{su} is the Kronecker delta. Note that contrary to [25] we *did not* use normalization of the dislocation density as we checked that in our case this does not lead to any improvement in model accuracy nor efficiency. Therefore, normalization was omitted for the sake of simplicity. The models were implemented using the AceGen code generator and the FEM simulations were performed using the AceFEM system [27, 28].

2.2. Berkovich indenter—contact formulation

The contact element has been implemented following the approach described in [22, 29]. The augmented Lagrangian method was applied to enforce frictionless contact constraints. The element was implemented using the aforementioned AceGen software. The essence of the implementation reported here (used already in [30] without explaining the details) is that the Berkovich shape and bluntness of the tip were both explicitly taken into account. The bluntness was achieved by using three parabolic cylinders and the rest of the indenter is assumed to consist of three planes. The function defining the shape $z = f(x,y)$ takes the following values:

$$\begin{cases} Cy^2, & \text{if } y \geqslant \frac{\sqrt{3}}{3}x \text{ and } y \geqslant -\frac{\sqrt{3}}{3}x \text{ and } y \leqslant x_0 \\ \frac{C}{4}\left(-\sqrt{3}x + y\right)^2, & \text{if } y < \frac{\sqrt{3}}{3}x \text{ and } x \geqslant 0 \text{ and } x \geqslant \sqrt{3}x - 2x_0 \\ \frac{C}{4}\left(\sqrt{3}x + y\right)^2, & \text{if } y < -\frac{\sqrt{3}}{3}x \text{ and } x < 0 \text{ and } y \geqslant -\sqrt{3}x - 2x_0 \\ -\sqrt{3}\left(-\sqrt{3}ahx + \frac{hy}{a}\right) - h, & \text{if } x \geqslant 0 \text{ and } y \leqslant \frac{\sqrt{3}}{3}x \\ \frac{\sqrt{3}\left(-\sqrt{3}hx - hy\right)}{a} - h, & \text{if } x < 0 \text{ and } y \leqslant -\frac{\sqrt{3}}{3}x \\ \frac{2\sqrt{3}hy}{a} - h & \text{otherwise} \end{cases} \tag{13}$$

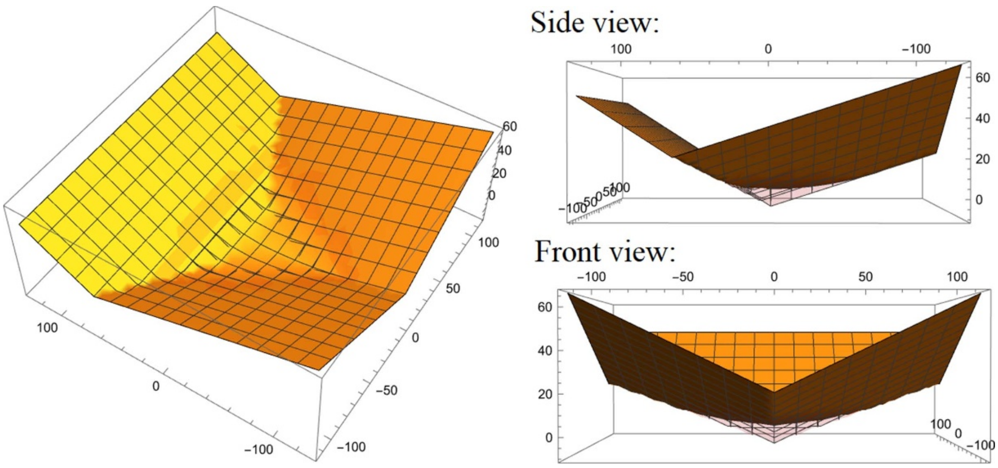

Figure 1. Visualization of the function defining the shape of the blunted Berkovich indenter together with the perfect Berkovich indenter.

and is visualized in figure 1. Note that the function $z = f(x, y)$ provides the z coordinate for every values of x and y coordinates, thus defining a 3D shape of the Berkovich indenter. The parameters a and h describe the perfect Berkovich indenter and are equal to 1486 nm and 200 nm, respectively. The parameters h, C and x_0 describe the tip bluntness and are calculated from the specified tip radius R:

$$h = R\left(\frac{1}{\sin\alpha} - 1\right), \tag{14}$$

$$C = \frac{\tan^2 90^o - \alpha}{4h}, \tag{15}$$

$$x_0 = \frac{\tan 90^o - \alpha}{2C}, \tag{16}$$

where α is the angle between the vertical axis and the axis of the side equal to:

$$\alpha = \text{ ArcTan}\left(\frac{a\sqrt{3}}{6h}\right). \tag{17}$$

The FEM mesh used in indentation simulations is shown in figure 2. The mesh was generated using the ABAQUS software and consists of 8-noded hexahedral elements. The contact elements were generated by choosing the 4-noded quadrilateral elements on the upper surface that were inside a circle of radius 1200 nm. The simulations of indentation were conducted by prescribing the upward displacement of the lower surface of the mesh while the position of the indenter was kept fixed. This is equivalent to moving the indenter downward with fixed lower surface of the body.

2.3. Parameter calibration

The starting set of parameters was taken from [24, 25]. In order to obtain the correct parameters of the investigated material in the virgin state, we performed simulations of uniaxial tension

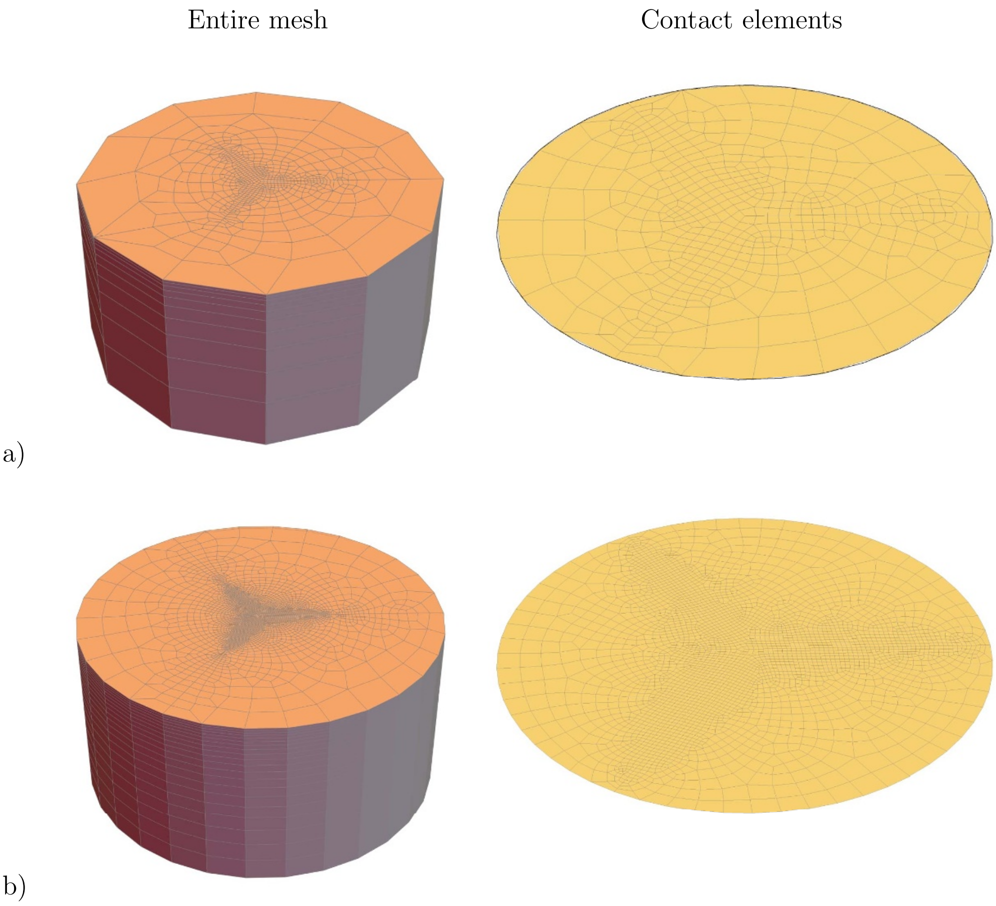

Figure 2. Finite element meshes of the whole domain and the contact elements (upper surface 4-noded quadrilateral elements inside a circle or radius 1200 nm): (a) coarse mesh and (b) fine mesh.

Table 2. The parameters used in the developed crystal plasticity formulation (the parameters established through calibration are shown in red, the other parameters were taken from [24, 25]).

C_{11}	C_{12}	C_{44}	μ	τ_0	n	b_D	$\rho_{D,0}$	κ	y_c	v_0
GPa	GPa	GPa	GPa	GPa	—	m	m/m^3	—	—	1/s
199.0	136.0	105.0	66.0	0.22	15	$2.54 \cdot 10^{-10}$	$1.6 \cdot 10^{12}$	15	24	0.001

and compared them against the experimental results. The simulations were conducted using the polycrystal consisting of 1000 grains subjected to periodic boundary conditions. Since the problem of matching only one simulated stress–strain curve with the experimental one is relatively simple, the fitting procedure was performed using a trial-and-error approach. The parameters changed in the calibration procedure are presented in table 2 in red. The stress–strain curves obtained in experiment and simulation are presented in figure 3.

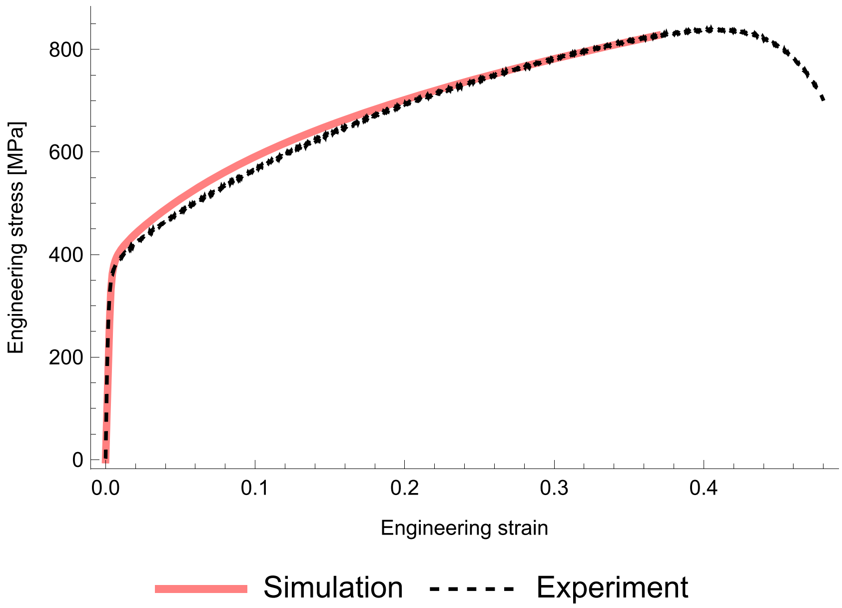

Figure 3. The stress–strain curves obtained in the simulations of the polycrystal compared against experimental data from [31].

3. Results

In simulations of indentation, we have used the parameters calibrated by fitting the stress–strain curves. Both FEM meshes show similar LD response, except that finer mesh provides smoother LD curve. Since the exact value of the tip radius was not measured, we started from the estimated value of R equal to 100 nm. It then appeared that the best agreement is obtained when using R equal to 150 nm. The results of the indentation simulations compared against the experimental data at various grains [32] are shown in figure 4. We again stress that the material parameters are exactly the same as in the simulation of tension. Therefore, the observed remarkable agreement is obtained only by fitting the radius of the Berkovich tip.

4. Discussion

4.1. The effect of the tip radius

In order to study the influence of the tip imperfection, we conducted simulations with different radii. Figure 5 presents the LD curves for radii equal to 50, 100, 150, 200, 250 and 300 nm. One can see that the higher value of the radius (the bigger the imperfection), the higher the load necessary to deform a material to a given penetration. This is consistent with the intuitive mechanistic understanding of the problem: infinitely sharp indenter penetrates the material easily since it only has to overcome the material resistance locally, while less and less sharp indenter compresses larger and larger material surface at the same time. Figure 6 presents the influence of tip radius on surface topography. As could be expected, the only noticeable difference between the imprints is the larger imprint area for the same depth in the case of bigger radius.

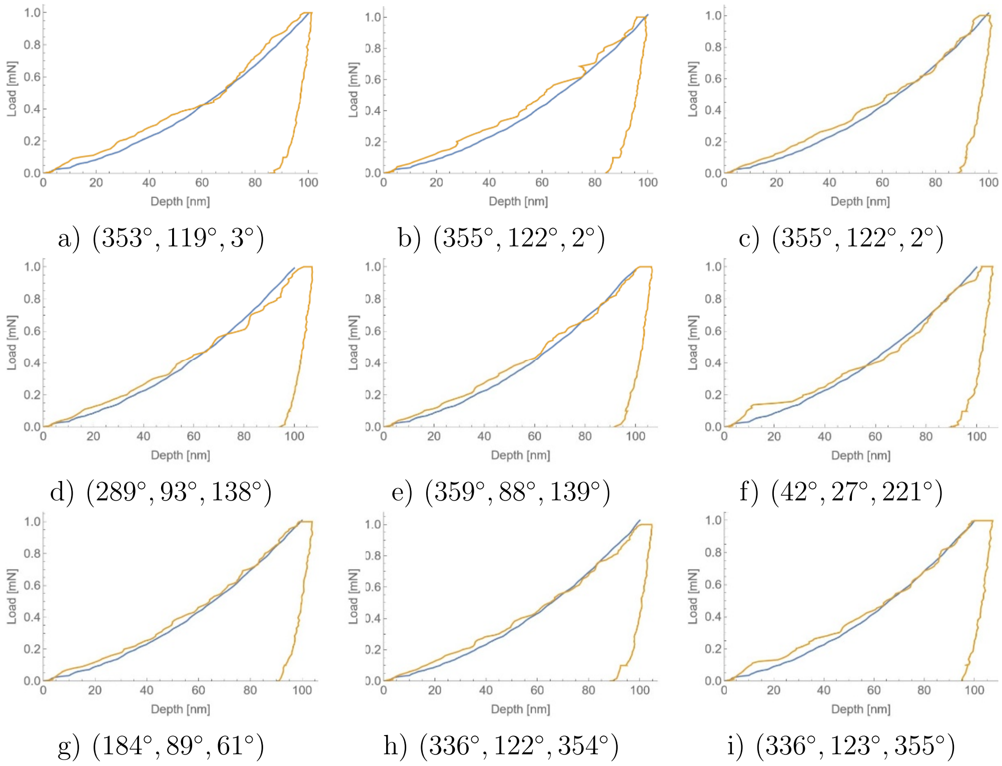

Figure 4. Load-displacement curves obtained in experiments [32] and simulations with the coarse mesh. The experiments and simulations have been performed for grains with orientation defined by Euler angles: (a) $(353°, 119°, 3°)$, (b) $(355°, 122°, 2°)$, (c) $(355°, 122°, 2°)$, (d) $(289°, 93°, 138°)$, (e) $(359°, 88°, 139°)$, (f) $(42°, 27°, 221°)$, (g) $(184°, 89°, 61°)$, (h) $(336°, 122°, 354°)$, (i) $(336°, 123°, 355°)$.

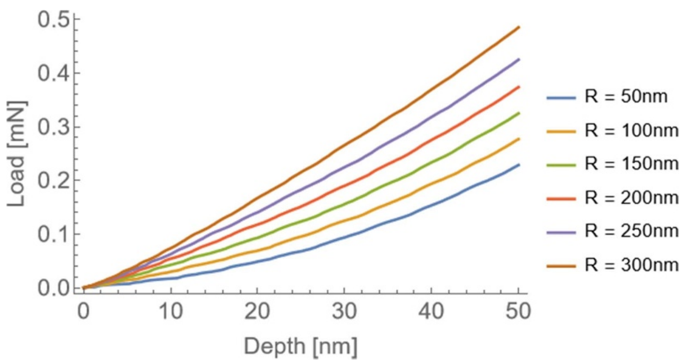

Figure 5. The influence of tip radius on the load-displacement curves.

4.2. The effect of crystal orientation

We have also checked what is the effect of crystallographic orientation on the resulting LD curves and surface topographies. Figure 7 presents the influence of tip radius on LD curves.

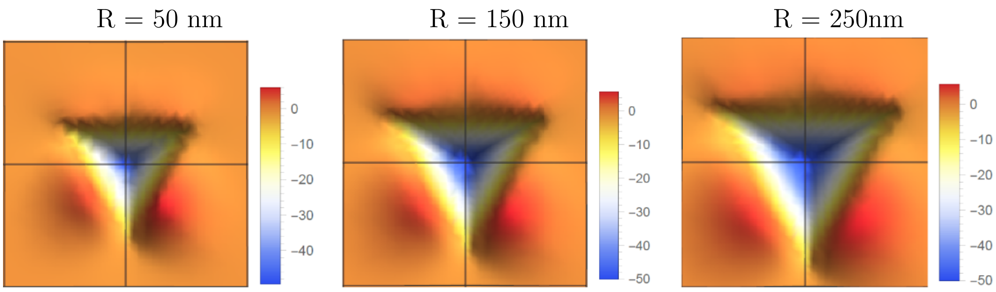

Figure 6. The influence of tip radius on surface topography. Note that all the surface plots were done at the same indentation depth.

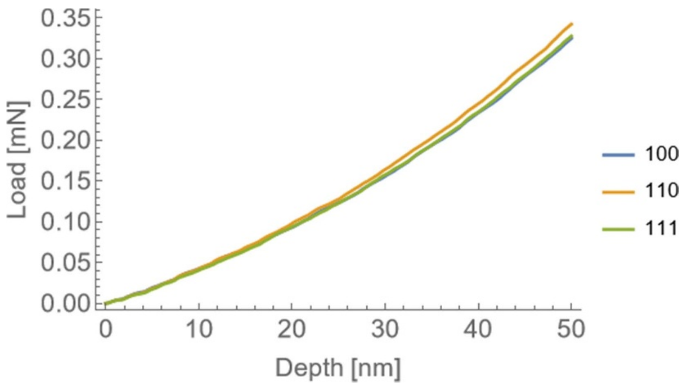

Figure 7. The influence of crystallographic orientation on load-displacement curves for Berkovich indentation ($R = 150$ nm) and crystal orientation: (a) 100, (b) 110 and (c) 111.

One can see that there is almost no difference for different crystallographic orientations. Similar conclusion was reported for axisymmetric conical indenter with imperfection in [22] (see figure 6). This can be explained by noting that these results concern austenitic stainless steel. This material has face centered cubic structure and deforms only by crystallographic slip. We expect that a different situation can occur in more plastically anisotropic material such as Ti, Mg, Zn or Zr alloys with hexagonal close packed crystallographic structure, see e.g. [33].

Even though, there is almost no influence of the crystallographic orientation on the load-penetration curve, it has a clear effect on the surface topography, cf figure 8. When indented with an axially symmetrical tip, the selected crystallographic orientations are characterized by four fold (cf figure 8(d)), two fold (cf figure 8(e)) and three fold (cf figure 8(f)) symmetry. These patterns cannot be fully revealed with Berkovich indentation (cf figures 8(a)–(c)), see also [34]). Nevertheless, one can still see considerable differences stemming from different crystallographic orientations.

4.3. The effect of friction

The dislocation density-based model applied in the current paper leads to rather computationally intensive simulations. Accounting for friction leads to further increase of computing time. Moreover, the specific value of the friction coefficient that should be used is unknown.

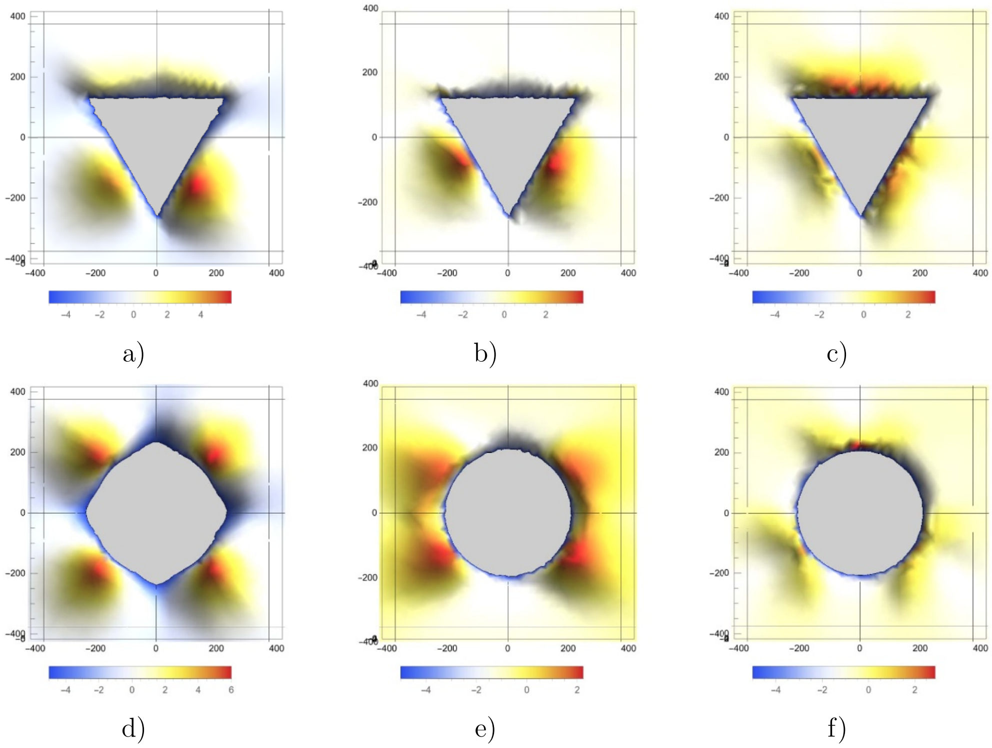

Figure 8. The influence of crystallographic orientation on surface topography for Berkovich indentation and crystal orientation: (a) 100, (b) 110 and (c) 111. For comparison, the results of spherical indentation for the same orientation are provided in (d)–(f) (d) 100, (e) 110 and (f) 111). To better visualise the surface patterns, the part of the surface inside the indent is hidden.

Therefore, frictionless contact was used in all simulations reported thus far. In the past, we have demonstrated that in the case of a standard crystal plasticity model and *spherical* indenter, friction affects the simulated LD curves only at depths that are unattainable at spherical indentation experiments, cf figure 12 in [23]. Namely, in the figure present in *op. cit.*, for a spherical indenter with radius = 200 microns, the effect of friction starts to be seen at around 100 microns. In the current paper, the maximum depth is much lower (100 nm), nevertheless, the question of validity of the applied frictionless approach was investigated, because both the shape of indenter and the crystal plasticity formulation were different than in [23].

Figure 9 presents the comparison of LD curves obtained in frictionless and Coulomb friction indentation simulations obtained using the coarser mesh (presented in figure 2(a)) and tip imperfection radius 50 nm. The comparisons have been done for both the simple crystal plasticity model reported in [23] (figure 9(a)) and for the dislocation-density based model reported here (figure 9(b)). The results for the simple crystal plasticity (figure 9(a)) show that there is very little impact of including friction on the LD curves. The results for the dislocation density based model (figure 9(b)) show that a little bit higher force level is attained at depth higher than 20 nm. However, even at the highest depth used in this paper (100 nm), the difference is still small (relative maximum error being equal to 5%). The error is comparable to the experimental scatter (cf figure 4). Therefore, using the frictionless approximation seems

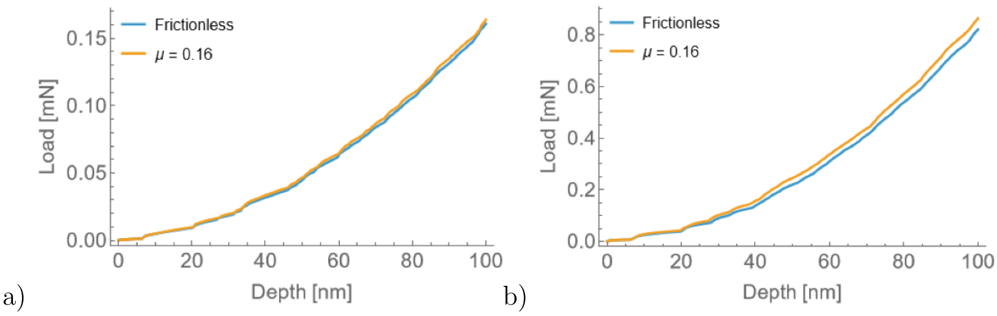

Figure 9. The influence of friction on load-displacement curves for: (a) simple crystal plasticity model as in [23] and (b) dislocation-density based model as described in the present paper. Simulations have been conducted for 100 orientation, coarser mesh (figure 2(a)) and tip imperfection radius equal to 50 nm.

to be a valid approach for the extremely small penetration depth (100 nm) considered in the submitted paper. Nevertheless, the approach should be reconsidered when simulating larger penetration depths or introducing other changes.

4.4. Geometrically necessary dislocations

Let us reiterate that the agreement between LD curves observed in figure 4 was possible using: (1) material parameters established by fitting *tensile* stress–strain curves, (2) accounting for tip imperfection. In other words, using parameters established in tension without accounting for tip imperfection would result in too low stress levels. This fact could be also possibly explained using the theory originally proposed by Nix and Gao [35]. According to this approach, the strain gradients occurring due to indentation are accommodated by so called geometrically necessary dislocations (GNDs). The presence of these dislocations is responsible for a part of an increase in strength of material. The density of GNDs is equal to the length of the circular GND loops divided by the volume containing them. Thus, as the length is proportional to the square of the depth and volume is proportional to its cube, the GND density is inversely proportional to depth which results in the observed size effect. The strain gradient theory was successfully applied to account for size effect in the case of spherical [36] and pyramidal [37] indentation. Note however, that the very small depth regime studied here (up to 100 nm) is essentially not covered by the classical Nix-Gao theory, see [38].

On the other hand, as noted in the Introduction (section 1), in many papers it was demonstrated that the increase of hardness with decreasing depth can partially result from the imperfect tip. This is also shown in figure 5, where the load (and thus also hardness) increases with increasing radius of tip imperfection. Neglecting the tip imperfection and accounting for the indentation size effect (ISE) while using perfectly sharp tip does not seem to be a valid approach, especially in the ultra-low indentation depth regime studied here. On the other hand, using the Nix-Gao based theory (ideally in the version tailored for extremely low depths, cf e.g. [39, 40]) *together* with proper treatment of the tip imperfection seems to be a reasonable path. This way of approaching the problem was already presented in some papers, see [41].

It seems that in order to rigorously solve the issues related to a competition between ISE resulting from GNDs and tip imperfection effects, one has to perform a joint experimental and modelling campaign as follows. First, one should consider a material whose properties are well known. Ideally this should be a big single crystal in order to get rid of any grain boundary effects. Then, independent experiments to find the mechanical properties (e.g. compression) should be carried out. Next, indentation experiments with pyramidal indenters with various tip imperfections should be performed. For each indenter, the exact tip geometry should be known beforehand, e.g. by AFM measurements. The material parameters should be calibrated based on experiments independent from nanoindentation. Then, simulations of nanoindentation should be performed. For those simulations, exact tip imperfection should be used. This is different from the approach presented here since in the current paper exact tip imperfection information was not provided and thus tip imperfection was assessed based on LD curves. In the proposed approach, using exact tip imperfection will enable verification whether the simulated LD curves agree with experimental data. If the LD curves do not agree, the validity of GND-based models accounting for ISE can be studied. However, such a rigorous study would require a consistent effort from both experimental and modelling groups and is clearly outside the scope of the current paper.

5. Conclusions

In this paper, the importance of accounting for tip imperfection when modelling Berkovich nanoindentation was higlighted. Therefore, the analytical function describing the shape of imperfect Berkovich indenter tip was proposed for the first time. The contact element using this function as well as dislocation density based model were both implemented using the AceGen software. Using the developed approach it was possible to perform simulations of Berkovich indentation and a perfect agreement with experimental data was obtained. It should be stressed that the parameters of the constitutive model were calibrated using the tensile experiment information only and no modification of these parameters was introduced when performing the simulations of Berkovich nanoindentation. Finally, the role of tip imperfection and crystallographic orientation were investigated.

Data availability statement

The data that support the findings of this study are openly available at the following URL/DOI: https://doi.org/10.5281/zenodo.15181083.

Acknowledgments

Sandra Musiał from IPPT PAN is acknowledged for sharing numerical data for stress–strain curves reported in [31]. Aneta Ustrzycka from IPPT PAN and Katarzyna Mulewska from NCBJ are acknowledged for sharing nanoindentation data reported in [32].

The publication was created within the framework of the project of the Minister of Science and Higher Education ‘Support for the activities of Centres of Excellence established in Poland under Horizon 2020’ under Contract No. MEiN/2023/DIR/3795.

Appendix

The form of the matrix h_{τ}^{su} is the following:

$$h_{\tau}=\begin{bmatrix} a1 & a2 & a2 & a4 & a5 & a5 & a3 & a5 & a6 & a3 & a6 & a5\\ a2 & a1 & a2 & a5 & a3 & a6 & a5 & a4 & a5 & a6 & a3 & a5\\ a2 & a2 & a1 & a5 & a6 & a3 & a6 & a5 & a3 & a5 & a5 & a4\\ a4 & a5 & a5 & a1 & a2 & a2 & a3 & a6 & a5 & a3 & a5 & a6\\ a5 & a3 & a6 & a2 & a1 & a2 & a6 & a3 & a5 & a5 & a4 & a5\\ a5 & a6 & a3 & a2 & a2 & a1 & a5 & a5 & a4 & a6 & a5 & a3\\ a3 & a5 & a6 & a3 & a6 & a5 & a1 & a2 & a2 & a4 & a5 & a6\\ a5 & a4 & a5 & a6 & a3 & a5 & a2 & a1 & a2 & a5 & a3 & a6\\ a6 & a5 & a3 & a5 & a5 & a4 & a2 & a2 & a1 & a5 & a6 & a3\\ a3 & a6 & a5 & a3 & a5 & a6 & a4 & a5 & a5 & a1 & a2 & a2\\ a6 & a3 & a5 & a5 & a4 & a5 & a5 & a3 & a6 & a2 & a1 & a2\\ a5 & a5 & a4 & a6 & a5 & a3 & a6 & a6 & a3 & a2 & a2 & a1 \end{bmatrix} \tag{18}$$

where the slip systems are defined as:

$$s1=\left(\bar{1}11\right)\left[0\bar{1}1\right],\quad s2=\left(\bar{1}11\right)[101],\quad s3=\left(\bar{1}11\right)[110], \tag{19}$$

$$s4=(111)\left[0\bar{1}1\right],\quad s5=(111)\left[\bar{1}01\right],\quad s6=(111)\left[\bar{1}10\right], \tag{20}$$

$$s7=\left(\bar{1}\bar{1}1\right)[011],\quad s8=\left(\bar{1}\bar{1}1\right)[101],\quad s9=\left(\bar{1}\bar{1}1\right)\left[\bar{1}10\right], \tag{21}$$

$$s10=\left(1\bar{1}1\right)[011],\quad s11=\left(1\bar{1}1\right)\left[\bar{1}01\right],\quad s12=\left(1\bar{1}1\right)[110] \tag{22}$$

and the components of the matrix h_{τ}^{su} are defined in table 1.

ORCID iD

Karol Frydrych https://orcid.org/0000-0002-9040-1523

References

[1] Berkovich E 1951 Three faceted diamond pyramid for micro-hardness testing *Ind. Diam. Rev.* **11** 129
[2] Harsono E, Swaddiwudhipong S, Liu Z and Shen L 2011 Numerical and experimental indentation tests considering size effects *Int. J. Solids Struct.* **48** 972–8
[3] He Y, Yang J, Ma Y, Dong P, Ma J, Xiong H and Li W 2024 Model for predicting temperature-dependent indentation yield strength and hardness considering size effects *Int. J. Solids Struct.* **298** 112881
[4] Kucharski S, Stupkiewicz S and Petryk H 2014 Surface pile-up patterns in indentation testing of Cu single crystals *Exp. Mech.* **54** 957–69
[5] Frydrych K, Dominguez-Gutierrez F, Alava M and Papanikolaou S 2023 Multiscale nanoindentation modelling of concentrated solid solutions: a continuum plasticity model *Mech. Mater.* **181** 104644
[6] Kucharski S, Maj M, Ryś M and Petryk H 2024 Size effects in spherical indentation of single crystal copper *Int. J. Mech. Sci.* **272** 109138
[7] Larsson P-L, Giannakopoulos A, Söderlund E, Rowcliffe D and Vestergaard R 1996 Analysis of Berkovich indentation *Int. J. Solids Struct.* **33** 221–48
[8] Liu M and Yang F 2013 Three-dimensional finite element simulation of the Berkovich indentation of a transversely isotropic piezoelectric material: effect of material orientation *Modelling Simul. Mater. Sci. Eng.* **21** 045014

[9] Wang Z, Zhang J, ul Hassan H, Zhang J, Yan Y, Hartmaier A and Sun T 2018 Coupled effect of crystallographic orientation and indenter geometry on nanoindentation of single crystalline copper *Int. J. Mech. Sci.* **148** 531–9
[10] Khvan T, Noels L, Terentyev D, Dencker F, Stauffer D, Hangen U, Van Renterghem W, Cheng C and Zinovev A 2022 High temperature nanoindentation of iron: experimental and computational study *J. Nucl. Mater.* **567** 153815
[11] Chen W, Li M, Zhang T, Cheng Y-T and Cheng C-M 2007 Influence of indenter tip roundness on hardness behavior in nanoindentation *Mater. Sci. Eng. A* **445** 323–7
[12] Sakharova N, Fernandes J, Antunes J and Oliveira M 2009 Comparison between Berkovich, vickers and conical indentation tests: a three-dimensional numerical simulation study *Int. J. Solids Struct.* **46** 1095–104
[13] Warren A and Guo Y 2006 Machined surface properties determined by nanoindentation: experimental and FEA studies on the effects of surface integrity and tip geometry *Surf. Coat. Technol.* **201** 423–33
[14] Kovář J, Fuis V and Tomáštík J 2020 Influencing the indentation curves by the bluntness of the Berkovich indenter at the FEM modelling *Acta Polytech. CTU Proc.* **27** 131–5
[15] Torres-Torres D, Muñoz-Saldaña J, Gutierrez-Ladron-de Guevara L, Hurtado-Macías A and Swain M 2010 Geometry and bluntness tip effects on elastic–plastic behaviour during nanoindentation of fused silica: experimental and FE simulation *Modelling Simul. Mater. Sci. Eng.* **18** 075006
[16] Krier J, Breuils J, Jacomine L and Pelletier H 2012 Introduction of the real tip defect of Berkovich indenter to reproduce with fem nanoindentation test at shallow penetration depth *J. Mater. Res.* **27** 28–38
[17] Čech J, Hauš P, Kovářík O and Materna A 2016 Examination of Berkovich indenter tip bluntness *Mater. Des.* **109** 347–53
[18] Sanchez-Camargo C-M, Hor A and Mabru C 2020 A robust inverse analysis method for elastoplastic behavior identification using the true geometry modeling of Berkovich indenter *Int. J. Mech. Sci.* **171** 105370
[19] Frydrych K and Kowalczyk-Gajewska K 2018 Grain refinement in the equal channel angular pressing process: simulations using the crystal plasticity finite element method *Modelling Simul. Mater. Sci. Eng.* **26** 065015
[20] Frydrych K, Kowalczyk-Gajewska K and Prakash A 2019 On solution mapping and remeshing in crystal plasticity finite element simulations: application to equal channel angular pressing *Model. Simul. Mater. Sci. Eng.* **27** 075001
[21] Asaro R J and Needleman A 1985 Texture development and strain hardening in rate dependent polycrystals *Acta Metall.* **33** 923–53
[22] Frydrych K 2019 Crystal plasticity finite element simulations of the indentation test *Comput. Methods Mater. Sci.* **19** 41–49
[23] Frydrych K and Papanikolaou S 2022 Unambiguous identification of crystal plasticity parameters from spherical indentation *Crystals* **12** 1341
[24] Han X 2012 Modeling of cavity swelling-induced embrittlement in irradiated austenitic stainless steels; modelisation de la fragilisation due au gonflement dans les aciers inoxydables austenitiques irradies *PhD Thesis* Ecole Nationale Superieure des Mines de Paris Univ. Paris, France
[25] Hure J, El Shawish S, Cizelj L and Tanguy B 2016 Intergranular stress distributions in polycrystalline aggregates of irradiated stainless steel *J. Nucl. Mater.* **476** 231–42
[26] Ling C, Tanguy B, Besson J, Forest S and Latourte F 2017 Void growth and coalescence in triaxial stress fields in irradiated FCC single crystals *J. Nucl. Mater.* **492** 157–70
[27] Korelc J and Stupkiewicz S 2014 Closed-form matrix exponential and its application in finite-strain plasticity *Int. J. Numer. Methods Eng.* **98** 960–87
[28] Korelc J and Wriggers P 2016 *Automation of Finite Element Methods* (Springer)
[29] Lengiewicz J, Korelc J and Stupkiewicz S 2011 Automation of finite element formulations for large deformation contact problems *Int. J. Numer. Methods Eng.* **85** 1252–79
[30] Frydrych K 2023 Modelling irradiation effects in metallic materials using the crystal plasticity theory—a review *Crystals* **13** 771
[31] Musiał S, Maj M, Urbański L and Nowak M 2022 Field analysis of energy conversion during plastic deformation of 310s stainless steel *Int. J. Solids Struct.* **238** 111411
[32] Nowak M , Mulewska K, Azarov A, Kurpaska Ł and Ustrzycka A 2023 A peridynamic elastoplastic damage model for ion-irradiated materials *Int. J. Mech. Sci.* **237** 107806

[33] Somekawa H and Schuh C A 2016 Effect of crystal orientation on nanoindentation behavior in magnesium *Metall. Mater. Trans. A* **47** 3227–34

[34] Eidel B 2011 Crystal plasticity finite-element analysis versus experimental results of pyramidal indentation into (0 0 1) fcc single crystal *Acta Mater.* **59** 1761–71

[35] Nix W D and Gao H 1998 Indentation size effects in crystalline materials: a law for strain gradient plasticity *J. Mech. Phys. Solids* **46** 411–25

[36] Ryś M, Stupkiewicz S and Petryk H 2022 Micropolar regularization of crystal plasticity with the gradient-enhanced incremental hardening law *Int. J. Plast.* **156** 103355

[37] Lee W B and Chen Y 2010 Simulation of micro-indentation hardness of fcc single crystals by mechanism-based strain gradient crystal plasticity *Int. J. Plast.* **26** 1527–40

[38] Zhang X and Zhang C 2023 Inconsistent nanoindentation test hardness using different Berkovich indenters *J. Mater. Res. Technol.* **25** 6198–208

[39] Huang Y, Zhang F, Hwang K, Nix W, Pharr G and Feng G 2006 A model of size effects in nano-indentation *J. Mech. Phys. Solids* **54** 1668–86

[40] Wang J, Volz T, Weygand S M and Schwaiger R 2021 The indentation size effect of single-crystalline tungsten revisited *J. Mater. Res.* **36** 2166–75

[41] Xiao X, Chen L, Yu L and Duan H 2019 Modelling nano-indentation of ion-irradiated FCC single crystals by strain-gradient crystal plasticity theory *Int. J. Plast.* **116** 216–31